Applied Surface Science Advances 27 (2025) 100736

Contents lists available at ScienceDirect

Applied Surface Science Advances

journal homepage: www.sciencedirect.com/journal/applied-surface-science-advances

Full Length Article

Advanced surface engineering of TZO nanostructures via irradiation technique for enhanced nitric oxide (NO) gas sensitivity

Gani Yergaliuly [a,b,*], Abylay Tangirbergen [a,b], Almagul Mentbayeva [c], Nurlan Amangeldi [b], Marat Kaikanov [d], Selim Acar [e], Zhumabay Bakenov [c], Baktiyar Soltabayev [a,*]

[a] *Advanced Sensors Laboratory, National Laboratory Astana, Nazarbayev University, Astana 010000, Kazakhstan*
[b] *L.N. Gumilyov Eurasian National University, Astana 010000, Kazakhstan*
[c] *Department of Chemical and Material Engineering, School of Engineering and Digital Sciences, Nazarbayev University, Astana 010000, Kazakhstan*
[d] *Department of Physics, School of Sciences and Humanities, Nazarbayev University, Astana 010000, Kazakhstan*
[e] *Department of Physics, Faculty of Science, Gazi University, Ankara 06560, Turkey*

ARTICLE INFO

Keywords:
Titanium-doped zinc oxide
Silar technique
Ion beam irradiation
Nitrogen monoxide detection
Surface morphology
DFT

ABSTRACT

This manuscript investigates the enhancement of gas sensing properties of titanium-doped zinc oxide (TZO) nanostructures using intense pulsed ion beam irradiation (IPIB). TZO nanostructures synthesized using the sequential ion-layer adsorption and reaction (SILAR) method were subjected to two different treatments: thermal annealing at 500 °C under nitrogen atmosphere and IPIB. The study investigates the morphological, structural, optical, electrical, and gas-sensing properties of TZO with a focus on the sensitivity and selectivity to nitrogen monoxide (NO) and other gases. The results show that both annealed (*a*TZO) and irradiated (*i*TZO) nanofilms exhibit enhanced root-mean-square (RMS) roughness, resulting in improved gas sensing performance. IPIB irradiation induced significant lattice distortions and defects, which played a critical role in the dramatic performance improvement of the *i*TZO sensors. In particular, *i*TZO demonstrated a remarkable 1300 % improvement in response to 100 ppm NO at 200 °C. Furthermore, Density Functional Theory (DFT) results revealed that NO gas exhibited a moderate adsorption energy on defective TZO material compared to pristine TZO. This research demonstrates the effectiveness of IPIB irradiation in improving TZO-based gas sensors, suggesting potential for environmental monitoring and industrial applications. Future studies may explore the scalability of this technique and its application to other metal oxide semiconductors to develop advanced gas sensors.

1. Introduction

Air pollution is a global concern caused by industrial activities, transportation, agriculture, and natural phenomena such as wildfires and volcanic eruptions [1]. One of the major sources of air pollution is the combustion of fossil fuels, which releases harmful compounds and particles into the atmosphere. These pollutants can be carried to long distances by the wind, affecting both urban and rural areas. In addition, industrial activities like manufacturing and construction emit nitrogen oxides (NO_x) and sulfur oxides (SO_x). These emissions contribute to smog and acid rain [2]. Transportation is another major contributor to air pollution, particularly in urban areas where traffic congestion is common. Cars, buses, and trucks emit pollutants such as carbon monoxide (CO), nitrogen monoxide (NO), and particulate matter (PM), which can have a significant impact on air quality [3].

Among the toxic gases, exposure to NO gas can cause serious health problems [4], especially for vulnerable populations. Short-term exposure can lead to irritation, while long-term exposure can lead to respiratory problems [5] and increase the risk of heart disease and stroke [6]. Despite governments and organizations taking measures [7] to reduce emissions, air pollution remains a severe problem.

The essential step in promptly combating air pollution is the qualitative and quantitative detection thereof, which provides real-time data on air quality and identifies sources of pollution [8]. Gas sensors are devices that can detect and measure the concentration of various gases in the air. Common types of gas sensors include electrochemical, catalytic, infrared, photoionization, and metal oxide sensors [9]. Among them, metal oxide semiconductor (MOS) gas sensors have several advantages as low cost, high sensitivity, fast response time, low power consumption, and long lifetime compared to other types of gas sensors

---

* Corresponding authors.
E-mail addresses: gani.yergaliuly@nu.edu.kz (G. Yergaliuly), baktiyar.soltabayev@nu.edu.kz (B. Soltabayev).

https://doi.org/10.1016/j.apsadv.2025.100736
Received 28 January 2025; Received in revised form 12 March 2025; Accepted 17 March 2025

[10]. Different types (TiO_2, WO_3, SnO_2, ZnO, etc.) of MOS are usually used, and each type has its specific characteristics. Therefore, the choice of sensing material will depend on the specific gas being measured and the application. Due to its unique properties such as piezoelectricity [11], high electron mobility (145–166 cm^2/Vs) [12], wide bandgap energy (E_g=3.37 eV, corresponding to 376 nm) for effective absorption and emission of ultraviolet (UV) radiation [13], ZnO semiconductors are often used in gas sensor applications.

However, ZnO-based gas sensors face limitations that can restrict their performance and practical applications. One significant challenge is their relatively high optimal operating temperature, which typically ranges from 260 °C to 400 °C [14]. This high temperature increases power consumption, making them less ideal for portable or battery-operated devices.

To address these challenges, researchers have explored various strategies to improve the performance of ZnO-based gas sensors, including optimizing operating temperatures, incorporating composite materials, and employing doping techniques [15,16], as demonstrated in our previous work [17]. In the paper, a sensor for NO gas based on porous ZnO structures doped with titanium (TZO) in the shape of a flower has been developed using the Sequential Ion Layer Adsorption and Reaction (SILAR) method. Out of all samples with various Ti dopant content (0 - 5 wt%), the TZO-1 sensor contains 1 wt% Ti exhibited exceptional sensitivity with a 45 % response to 100 ppm NO gas. These performances were observed at an optimal operating temperature of 220 °C. The sensor was stable, and selective to NO gas over other gases. Despite a significant improvement in NO gas sensitivity, these sensors still need to achieve higher sensitivity values at lower operating temperatures.

One of the main findings of recent years is the increase of the MOS's gas sensitivity by modifying the surface using irradiation. Multiple kinds of irradiation can be used to improve the gas sensitivity of MOS-based materials, including gamma rays [18], UV illumination [19], impact by electron beam [20], ion beam irradiation [21], etc. Each irradiation type can improve the surface area of ZnO-based materials [22], increase the number of active sites [23], modify its electronic properties [24], and boost its selectivity towards specific gases. For example, in a study by Maqsood R. Waikar et al. [25], the NH_3 perception response of ZnO thin films increased 5 times after gamma irradiation at a dose of 30 kGy. The study by Gaoda Li et al. [26] finds that UV light leads to a more significant increase in surface state density and surface band bending, contributing to enhanced sensitivity when NO_2 is introduced. In the next work [27] the authors revealed the formation of oxygen vacancies on the surface of gas sensors by irradiating ZnO nanoparticles with Xe ions. As a result of this study, it is reported that the irradiated (irradiation dose: 1×10^{15} $ions/cm^2$) ZnO sensor shows almost 3.5 times high response, outstanding selectivity, and good reproducibility to NO_2 gas at 200 °C.

Based on the abovementioned data, we propose using an intensely pulsed ion beam (IPIB) [28] as a novel approach to enhance the gas-sensitive properties of TZO sensors. IPIB is an advanced method [29] that utilizes high-current ion beam pulses to redesign material properties, offering numerous advantages such as precise control of ion dose and energy [30] inducing lattice distortions and defects, and increasing surface area and porosity, which enhance gas adsorption and desorption processes [31]. Additionally, this irradiation technique preserves the material's structural integrity, making it highly suitable for improving gas sensors. In this study, the surfaces of TZO nanostructures were modified using high current density IPIB (proton ions). Rapid ion exposure (*i*TZO), functioning as a form of heat treatment, was compared to conventional thermal annealing at 500 °C in a nitrogen atmosphere (*a*TZO) to evaluate their respective effects on the NO gas sensitivity of unannealed TZO. Systematic analyses of the morphological, structural, optical, electrical, and gas-sensitive characteristics of the TZO samples demonstrated that both processing methods produced crystalline, porous thin films with increased root mean square (RMS) surface roughness and active surface area (see **Fig. S1** in Supporting Information (SI)), which directly improved the NO gas response of the TZO nanostructures. Furthermore, a comparison of the pristine and defective TZO material towards NO gas adsorption is analyzed using Density Functional Theory (DFT) modeling.

2. Experimental and theoretical part

2.1. Materials

Zinc chloride $ZnCl_2$ (≥98 % purity) used as the zinc source, titanium tetraisopropoxide $Ti\{OCH(CH_3)_2\}_4$ (97 % purity) used as the doping precursor, and ammonia NH_4OH (25–30 % concentration) used to adjust the solution pH were provided by Sigma-Aldrich. The primary solution for depositing thin films using the SILAR method was prepared by dissolving $ZnCl_2$ in distilled water. NH_4OH solution with a pH of approximately 10.5 was added drop by drop to form a complex of zinc and ammonia $[Zn(NH_3)_4]^{2+}$. For depositing TZO structures, a Ti/Zn molar ratio of 1.0 % was added separately to the previously prepared $[Zn(NH_3)_4]^{2+}$cationic solution. The solution was stirred at room temperature (~25 °C) for one hour.

2.2. Fabrication of TZO films

First, microscope slides (substrates) were cut into pieces measuring 5 mm in width and 7 mm in length. The prepared glass substrates were then ultrasonically cleaned using soapy water, distilled water, acetone, and a 1:1 ethanol-water mixture to eliminate organic residues. Finally, they were dried with nitrogen gas. Initially, a 99.999 % pure gold (Au) target and an aluminum mask were used to deposit ~150 nm thick interdigitated transducer (IDT) electrodes onto substrates via physical vapor deposition (PVD). The Au contact metal structure featured two interdigitated electrodes, each comprising four rods. Each rod measured 2.5 mm in length and 45 μm in width, with a spacing of 90 μm between them. The active area of the TZO sensor was around 0.3 cm^2 [17].

To prepare nanostructured TZO, one cycle (Fig. 1, **Step 1**) of the SILAR method includes four successive steps [32]. First, the substrate with Au IDT is immersed in a ZnOH mixture at room temperature (RT ~25 °C) for 15 s, which leads to the formation of a thin liquid film containing Ti-Zn ammonia complex ions (1 wt% Ti) on the surface of the substrate. Then the substrates are immersed into the 2nd beaker of hot (90 °C) distilled water (DW) for 7 s. The hot water rinse step is used as an anion source and is critical for the formation of oxide compounds [33,34]. After this, the thin film created on the surface of the substrate is air-dried for 60 s. Finally, the substrate is rinsed in a separate beaker for 30 s to remove larger TZO particles loosely bound to each other and the substrate. By completing this series of steps, one SILAR cycle is completed to prepare the thin film. Nanostructured TZOs are prepared by repeating this cycle for a total of 40 SILAR cycles. A more complete understanding of the deposition process, including detailed illustrations, was presented in our previous publications [17,35].

2.3. Annealing and irradiation by IPIB

To obtain annealed *a*TZO, the synthesized TZO films were placed in a tube furnace in N_2 medium for 2 h at a temperature of 500 °C.

IPIB irradiation experiments were conducted at Nazarbayev University on the Innovative Nazarbayev University's Research Accelerator "INURA" [36]. INURA is an ion beam accelerator utilizing pulsed-power architecture. The IPIB consisted mostly of protons with a peak kinetic energy of up to 280 keV and a pulse duration of 100 ns at full-width half maximum (FWHM), while the beam current density was 12 A/cm^2 (**Fig. S2** in SI). Corresponding beam fluence was $8{\cdot}10^{12}$ cm^{-2}. The beam spot size in a treatment region was about 5 cm in diameter per single pulse. All the samples were irradiated by a single pulse of proton beam. The impact of a single ion beam pulse within ~ 200 ns brings about an ultra-rapid annealing process (~600–700 °C within microseconds) [37],

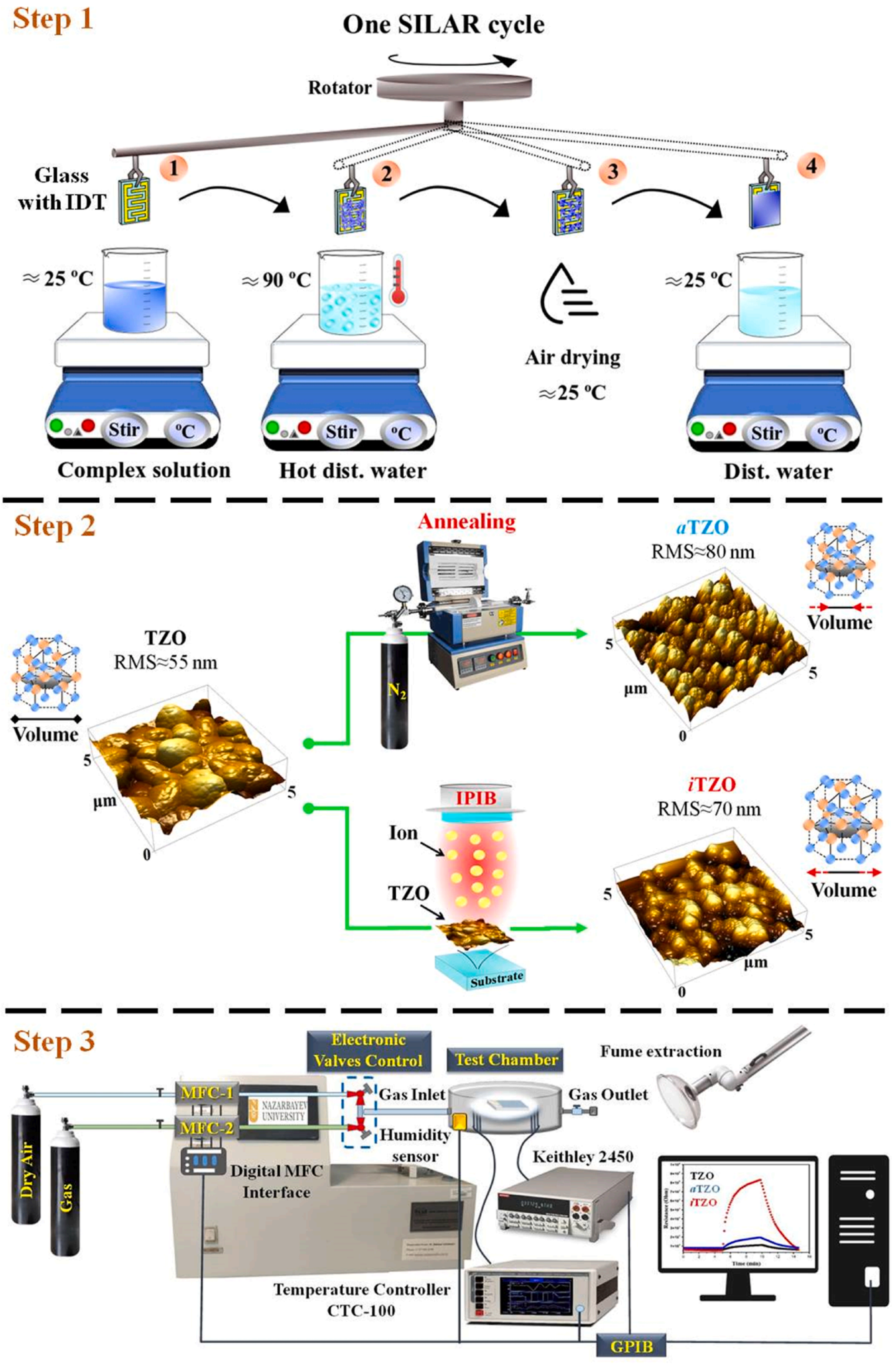

Fig. 1. Step-by-step illustration of the experimental workflow, including synthesis of TZO nanostructures, thermal and ion treatment, and gas sensing experiments for NO detection.

involving a heating phase lasting hundreds of nanoseconds, followed by cooling throughout microseconds [38]. Fig. 1 (**Step 2**) schematically illustrates the alternative treatment of TZO films by annealing and irradiation and their effect on the films with RMS values obtained on a SMART SPM 1000 atomic force microscope (AFM).

2.4. Characterization

In addition to the morphological properties listed above using AFM and scanning electron microscope (SEM) ZEISS Crossbeam 540, crystalline properties were investigated using X-ray diffraction (XRD) analysis on Rigaku SmartLAB. The optical properties of thin films were measured using the Nicolet iS10 Fourier-transform infrared (FT-IR) spectrometer an ultraviolet-visible (UV–Vis) spectrophotometer (Evolution 3000, Thermo Fisher) in the λ-wavelength range of 330–600 nm. Photoluminescence (PL) spectra were obtained using a spectrometer (FLS 1000, Edinburgh Instruments) with a 405 nm laser. The electrical parameters (conductivity, resistivity, mobility, etc.) of the TZO samples were extracted using a Hall measuring system (HMS-5500) with 0.53 T magnetic field and Keithley-2450 at RT. The surface chemistry of the films was studied by X-ray photoe spectroscopy (XPS).

2.5. The gas-sensitivity measurements of TZO sensors

Gas sensing measurements (Fig. 1, **Step 3**) were carried out utilizing our gas measurement system [39] on the sensors prepared in their original state. The sensor under evaluation was placed within a voluminous chamber ($V = 125$ cm^3), wherein the specific gas of interest was introduced via gas needle tubing connected to mass-flow-controller (MFC) connectors. Sensitivity (S) for the developed gas sensors was computed based on the relative alteration in sensor resistance between the ambient air (R_{air}) and the target gas (R_{gas}), as expressed by the equation $S\ (\%) = [(R_{gas}\text{-}R_{air})/R_{air}] \times 100$.

2.6. Density functional theory calculations of TZO materials

In this study, DFT calculations were employed to analyze the structural modifications induced by proton irradiation. The projected augmented wave (PAW) method [40,41] was utilized to accurately model quantum mechanical interactions. All simulations were conducted using the Vienna Ab initio Simulation Package (VASP-6) [42–44]. Initially, the non-polar ZnO (100) surface was constructed with Ti doping by substituting Zn atoms on the surface. Structural relaxation used the Generalized Gradient Approximation (GGA) with the Perdew-Burke-Ernzerhof (PBE) exchange-correlation functional. The PBE functional is widely recognized for its precise representation of exchange and correlation effects among electrons, making it a suitable choice for this study. The van der Waals (vdW) forces [45–47] within the surface and gas are accounted by the DFT-D2 method by Grimme [48]. A vacuum slab of 20 Å was implemented to prevent interactions between periodic images. For geometry optimization, a plane wave cut-off energy of 500 eV and a k-point mesh of (6 × 6 × 1) within Γ-centered scheme were utilised. During relaxation, atomic positions were fully optimized until the force on each atom was reduced to below 0.01 eV/Å between consecutive ionic steps, with the self-consistent electronic energy converging to $<10^{-6}$ eV. The maximum number of iterations is 300, which is enough to reach the required accuracy. To understand the effect of defect creation on gas adsorption, oxygen and zinc vacancies were created on the Ti doped ZnO (100) surface. The energy of NO gas adsorption was calculated on both pristine and defective surfaces as illustrated in formula 1:

$$E_{ads} = E_{surf/gas} - \left(E_{gas} + E_{surf}\right) \tag{1}$$

where, $E_{surf+gas}$ represents the total energy of the substrate-gas molecule complex, E_{surf} and E_{gas} correspond to the total energies of the pristine substrate and the isolated gas molecule, respectively. A negative E_{ads} value indicates a favorable or exothermic adsorption of the target gas on the substrate, whereas a positive value suggests repulsive interactions.

3. Results and discussion

3.1. SEM surface imaging

Improving the optical-electrical properties by changing the surface and structure of ZnO through doping significantly impacts gas detection efficiency. It is a key direction in the development of sensing devices and gas detectors [49]. Primary TZO (1 % Ti-doped ZnO) was modified by two processing techniques: thermal annealing (*a*TZO) and ion implantation (*i*TZO). One of the powerful, internationally recognized methods for studying the surface structures of materials with high resolution is SEM. The SEM analyses were performed and the results are shown in Fig. 2.

Fig. 2(a) shows the SEM image of bare TZO, which consists of nearly spherical almond-shaped particles with no distinct particle size distribution. **Fig. 2(b) and (c)** show the SEM images of annealed aTZO and irradiated iTZO nanostructures, respectively. The main difference is that in the irradiated sample, in addition to the primary TZO, there are tiny secondary TZO due to ion irradiation of the sample. These small particles increase the sensor's surface area and may affect the sensor behavior of the final product. Additional AFM analysis shown in **Fig. S1** (SI) also confirms the significant change in the roughness and grain size of TZO after annealing and IPIB irradiation. The changes in TZO sensor properties are further analyzed using XRD system (Rigaku SmartLAB) with Cu Kα radiation (λ = 1.5406 Å).

3.2. XRD analysis

Thus, SEM images showed that treatment with thermal annealing and IPIB irradiation significantly changes the surface of the TZO film. It is important to note that such structural changes due to two different techniques can lead to saturation of defects and dislocations. They are subsequently promoting recrystallization [50] or amorphization [51] of the sample's top layer. In this regard, XRD analysis was performed to obtain information about the crystallinity of the films. Fig. 3 (a,b) shows X-ray patterns of TZO, in which the peaks at 2θ - 31.4 34.1, 35.8, 47.1, 56.2, 62.5, and 67.7° refer to the lattice planes (100), (002), (101), (102), (110), (103), and (112) hexagonal zincite structure of ZnO nanoparticles, respectively (JCPDS, No36–1451). The findings demonstrate that the produced items were composed entirely of pure phases. No diffraction peaks were detected that were associated with impurities in the XRD pattern, confirming the exceptional purity of the synthesized material.

Fig. 3a indicates that after annealing and exposure to IPIB, the intensities of the main lattice peaks (100, 002, and 101) change. Fig. 3b depicts the shifts of the spectra, as well as the full width-half maximum (FWHM) of one of the central peaks (002) of TZO films. These spectrum shifts can be caused by various inconsistencies in the crystal lattice, including the formation of defects, and transformations in the size and reorientation of crystals [52]. In turn, reorientation effects lead to modifications in the average crystal size (D), dislocation density (δ), lattice parameters ($a = b$, c), strain (ε), and volume (V), which are outlined in Table 1.

The average D of the TZO particles can be obtained from the Debye–Scherrer formula [53]:

$$D = \frac{0.94\lambda}{\beta\cos\theta} \tag{2}$$

where 0.94 is the spherical shape constant, λ is the wavelength (1.5406 Å) of X-ray, and β is FWHM in radian. The $a = b$, c, and interplanar d spacing are calculated using the relationships obtained from the (002)

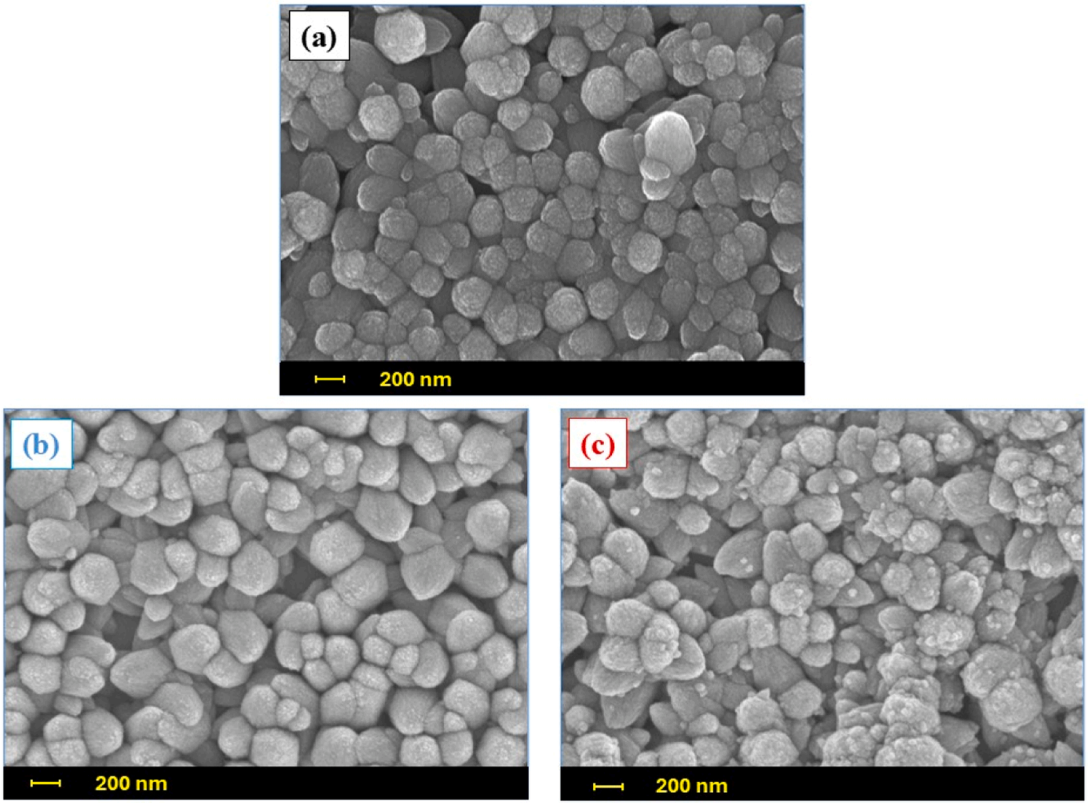

Fig. 2. SEM images of (a) pristine TZO, (b) annealed TZO (*a*TZO), and (c) ion-irradiated TZO (*i*TZO).

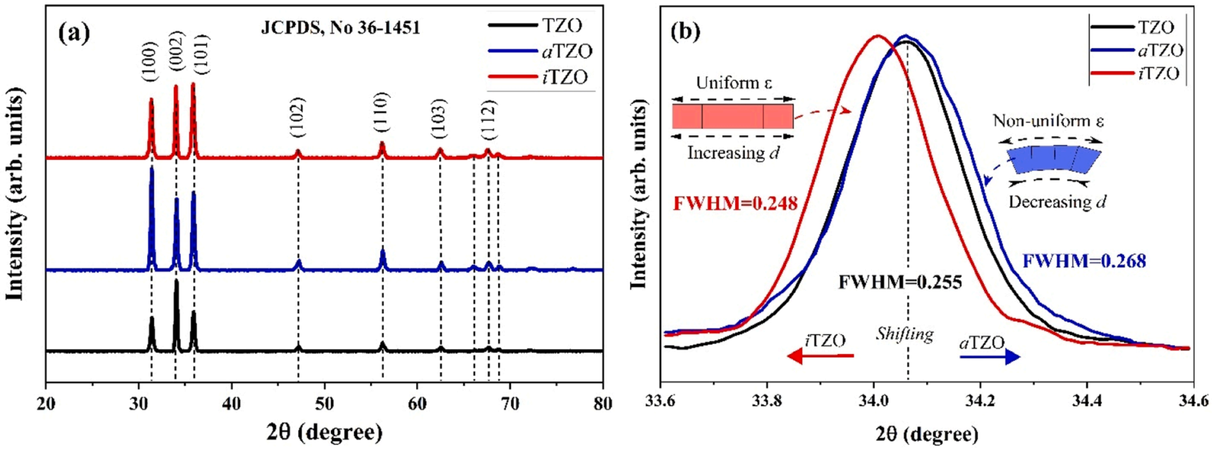

Fig. 3. (a) XRD patterns, and (b) - relation of (002) lattice plane of TZO, *a*TZO, and *i*TZO films.

Table 1
Structural parameters of TZO, *a*TZO, and *i*TZO thin films XRD patterns.

Sample	$2\theta_{(002)}$	D (nm)	ε (10^{-3})	δ (10^{-4} nm^{-2})	V (Å^3)	a/c	Lattice constants (Å)	
							a = *b*	c
TZO	34.06	34.046	3.63	8.63	41.402	0.58595	3.037	5.183
*a*TZO	34.07	32.381	3.82	9.54	41.366	0.58587	3.036	5.182
*i*TZO	34.01	35.002	3.54	8.17	41.580	0.58582	3.041	5.191

diffraction peak:

$$a = b = \frac{\lambda}{\left(\sqrt{3}\sin\theta\right)}\quad c = \frac{\lambda}{\sin\theta},\quad d = \frac{c}{\sqrt{h^2 + hk + k^2}} \tag{3}$$

where *h* and *k* are the Miller indices.

In the context of a hexagonal structure, the volume *V* of the unit cell can be determined through the expression:

$$V = 0.866 \times a^2 \times c \tag{4}$$

The Williamson-Hall analysis based on X-ray line broadening offers an approach for determining the average dimension of coherent diffracting regions as well as strain [54]. The broadening of peaks caused by ε and δ originate from crystal defects and distortions, and this effect can be quantified through the following correlations:

$$\varepsilon = \frac{\beta}{4\tan\theta}, \qquad \delta = \frac{1}{D^2} \tag{5}$$

From Table 1, it can be seen that during the thermal annealing of TZO, a structural rearrangement [55,56] of the crystal lattice occurs with a decrease in the d. Despite the decrease in V due to thermal effects, the ε and δ increase in the TZO film. The rapid IPIB's thermal effect decreases ε and δ by expanding the V along the c-axis. In turn, an increase in V leads to an upsurge in the *d, a,* and *c* parameters. Based on this, it can be assumed that IPIB irradiation promotes the ordering of the crystal structure of TZO, making it more contained.

3.3. Optical and electrical properties of TZO films

The quality of transmittance (in the wavelength range from 4000 cm^{-1} to 400 cm^{-1}) and absorbance (300–600 nm) were analyzed using FT-IR and UV–Vis spectroscopy, respectively. This was performed to evaluate the composition and potential interactions between components of the TZO films. The FT-IR spectra of TZO, *a*TZO, and *i*TZO are shown in Fig. 4a.

For primary TZO, sharp fronts are observed in the 400–600 cm^{-1} range and can be attributed to the Zn-O stretching mode [57]. In the 1000–600 cm^{-1} range, Zn-OH vibrations are predominantly present [58]. The broad absorption peaks around 3312 cm^{-1} and 3460 cm^{-1} correspond to the normal O—H stretching vibrations [59] on the surface of Zn-Ti-O nanoparticles. These vibrations may be related to the moisture content of the surrounding atmosphere. The presence of $C = O$ (~2160, ~2018 and ~1731 cm^{-1}) [60,61], C—O (~1255 cm^{-1} [62], and CO_2 [63] bonds explain the absorption peaks observed in the 1255–2400 cm^{-1} range. This is probably due to the absorption of atmospheric CO_2 by the metal cations of the equipment during analysis [64]. However, as a result of long annealing, for *a*TZO these peaks decrease, including the Zn–OH stretching vibrations (~600–990 cm^{-1}). Exposure to ion irradiation by IPIB (*i*TZO), on the contrary, promotes the formation of new stretches such as C—H (~2921 cm^{-1}) [65]. Considering that protons (hydrogen nuclei) are used as intense irradiating ions, we can conclude that they act to strengthen the Zn-OH and C—H bonds involving hydrogen atoms.

Fig. 4b shows the acquired UV–Vis absorption spectra of the prepared TZO thin films from 330 to 600 nm. The inset of the figure shows Tauc plots for TZO, *a*TZO, and *i*TZO, relating the absorption coefficient α to the photon energy $h\nu$. The band gap values for the specimens were determined using the established Tauc equation as follows [66]:

$$(\alpha h\nu) = A\left[h\nu - E_g\right]^n \tag{6}$$

In the aforementioned equation, α represents the absorption coefficient, h stands for Planck's constant, ν denotes the incident photon frequency, A is a constant, and E_g represents the bandgap energy. The index n's value was set to 1/2, indicating directly allowed transitions. Notwithstanding the significant effect of IPIB irradiation on the morphological characteristics of TZO films, the E_g widths changed minimally, stably maintaining a value of about 3.00 eV. Nevertheless, it is appropriate to emphasize that the E_g of the *a*TZO is 2.93 eV, which is less than the initial TZO, whose E_g is around 3.01 eV. The value of E_g also decreases in the case of *i*TZO and is equal to 2.97 eV. A sharp decrease in the optical density of the films in the visible region ($\lambda > 400$ nm) indicates the high transparency of the films in this region.

It is worth noting that arrays of primary TZO films demonstrate multidirectional intensity distributions in the spectrum's UV part (up to 400 nm). This can be explained by the presence of morphological inhomogeneities in the structure of the TZO, which possibly contains impurities that appear in the spectrum as fluctuation inclusions [67]. However, after thermal annealing of the *a*TZO, the intensity distribution becomes smooth and uniform over the entire measurement range. The IPIB irradiation had the same significant effect on the *i*TZO.

The effects of irradiation on the mobility and conductivity of TZO films were tested using a Hall measurement system at RT. Ohmic contacts were established by soldering lead to the four corners of square-shaped samples (1 cm x 1 cm). The magnetic field strength was set to 0.53 T, and a current of 1 μA was applied to all films. Hall measurements were repeated many times for each TZO film to ensure the reliability of the measurements. Hall's results are shown in Fig. 5a.

The results indicate a significant influence of ion irradiation on the electrical conductivity of TZO films. Specifically, it should be noted that due to ionic modification of the surface, the mobility and concentration of charge carriers in the *i*TZO sample increased tens of times compared to the original characteristics. Such improvements open up prospects for further testing of the resulting gas sensors for the presence of various toxic gases. The current-voltage (I-V) characteristic data were obtained using a Keithley-2450 and are presented in Fig. 5b.

Graphs of the I-V characteristics of all films showed linear dependences when voltage was applied between −3.0 and 3.0 V. The average resistance value of the TZO films within this electrical voltage was R_{TZO} ~10^8 Ohms. Due to the increase in the concentration of carriers and structural defects, the resistances of *a*TZO and *i*TZO decrease significantly by R_{aTZO} ~10^7 and R_{iTZO} ~10^5 Ohms, respectively. Thus,

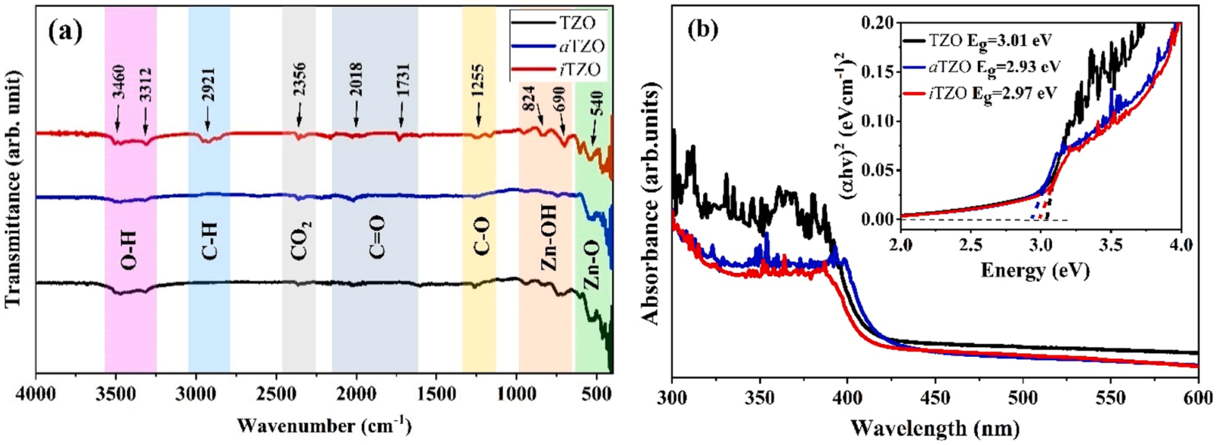

Fig. 4. **(a)** FT-IR transmittance of pristine, thermally annealed, and irradiated TZO, (b) UV–vis absorbance of TZO films.

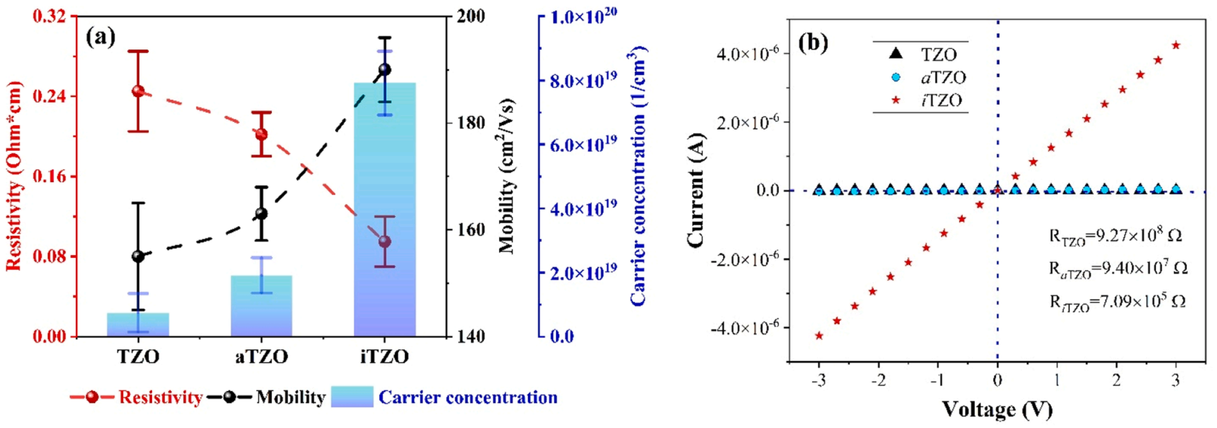

Fig. 5. (a) Hall measurement results, and (b) I-V characteristics of TZO films.

according to electrical measurements, thermal annealing and ion implantation of IPIB can effectively adjust and enhance surface resistance, decreasing it significantly (by tens of times) compared to the original TZO state.

3.4. XPS results

XPS is a highly efficient surface analysis method that provides additional data on the chemical composition of the sensor material's surface [68]. In addition, XPS analysis is very useful for analyzing and detecting oxygen vacancies, which play an important role in improving gas detection performance, as well as for an in-depth explanation of the gas detection mechanism in gas sensors [69]. Thus, to study the relationship between oxygen vacancies and gas sensing characteristics, XPS analysis was carried out, and Fig. 6 shows a high-resolution scan of the O1 s singlet peak. In this regard, all elements zinc, titanium, and oxygen showed agreement in photoemission characteristics in terms of main energy levels and spin-orbit splitting.

As shown in **Fig. 6(a-c)**, the O 1 s peaks were decomposed into their component components using a Gaussian curve fitting. In addition, peaks after deconvolution are shown for pristine TZO, *a*TZO, and *i*TZO, respectively. In all cases, the O1 s peak can be decomposed into three components: O1 (denoting lattice oxygen, ~530 eV), O_2 (denoting oxygen vacancies, ~531 eV), and O_3 (denoting the hydroxyl (OH) group,

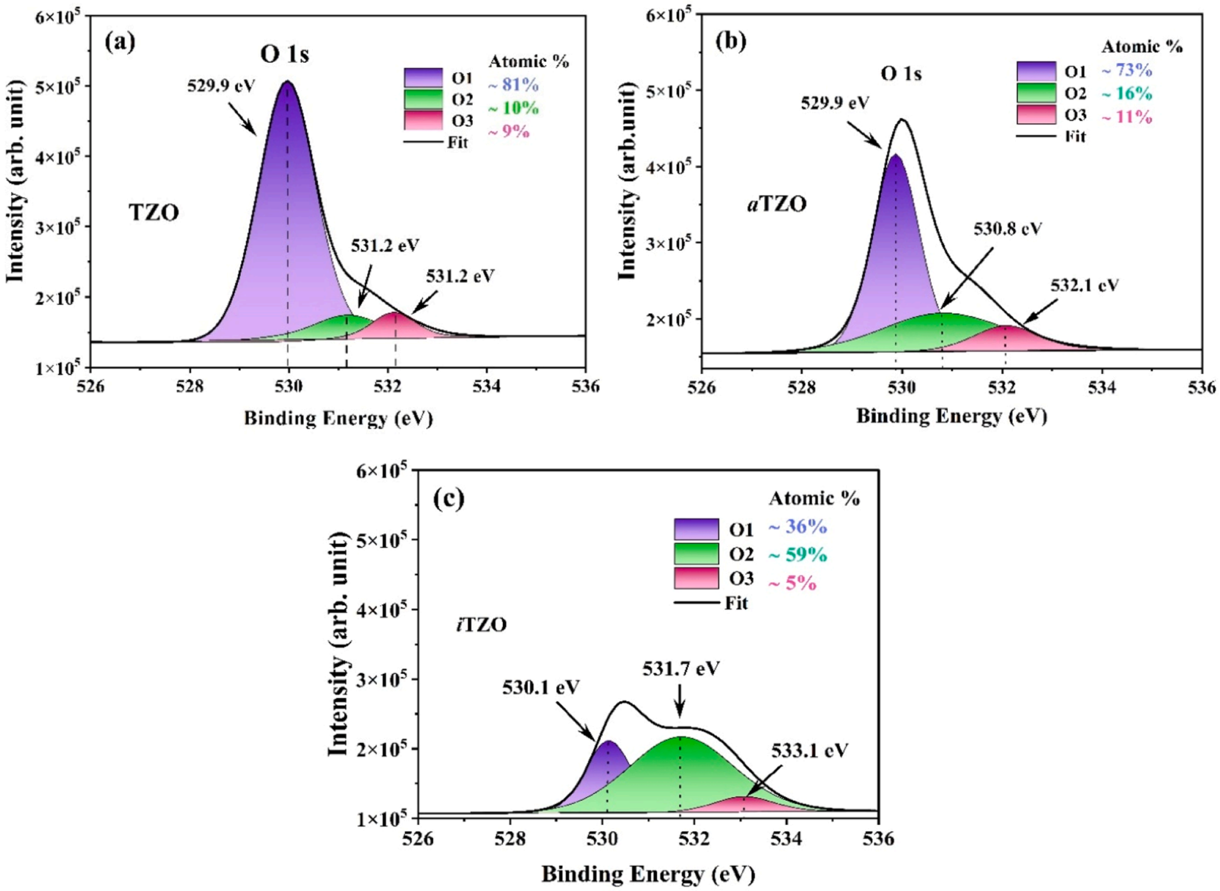

Fig. 6. XPS O-1 s spectra of the (a) TZO, (b) *a*TZO (c) *i*TZO films.

~533 eV) [70]. The atomic oxygen concentrations for the TZO, *a*TZO, and *i*TZO sensors were ~10 %, ~16 %, and ~59 %, respectively. The formation of oxygen defects such as oxygen vacancies, is explained by changes in the atomic concentration of oxygen in ZnO. The atomic concentration of oxygen decreases with the use of irradiation (pulse plus), which indicates an increase in the number of oxygen vacancies. These oxygen vacancies play a vital role in enhancing the gas-sensing performance of irradiated ZnO-based gas sensors [71].

3.5. Gas measurement results of TZO sensors

Fig. 7a shows a graph that illustrates the response percentage of TZO sensors as a function of temperature, where three different sensors are compared: TZO, *a*TZO, and *i*TZO. Notably, the *i*TZO sensor shows a

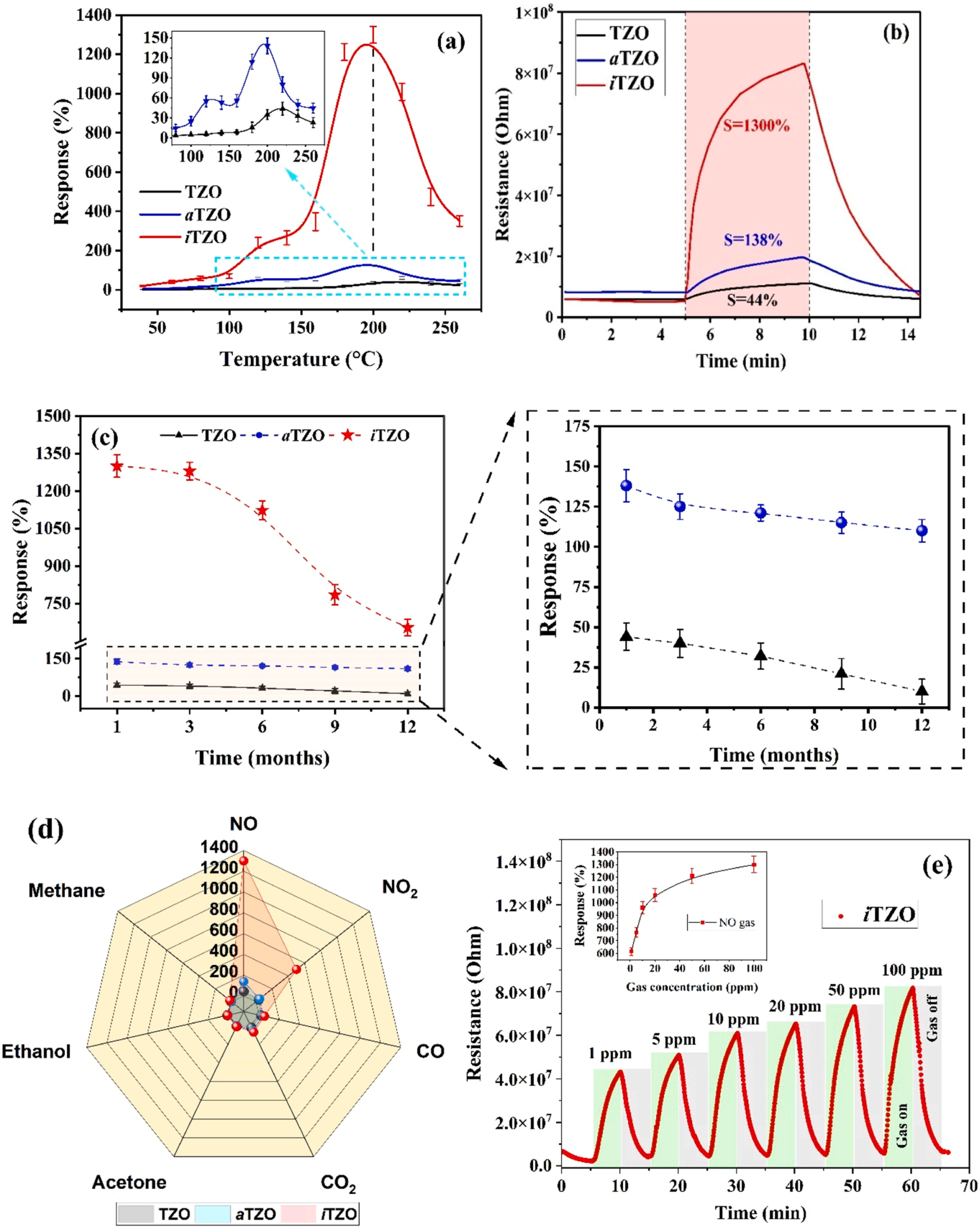

Fig. 7. (a) The gas response to 100 ppm NO gas versus operating temperature; (b) Response-transient plots in terms of the actually measured resistance at 200 °C; (c) stability and (d) selectivity performance of TZO, *a*TZO, and *i*TZO sensors; (e) dynamic measurements of *i*TZO sensor.

sharp peak in response, reaching approximately 1300 % around 200 °C before dropping dramatically. In contrast, the TZO and *a*TZO sensors exhibit much lower and flatter responses across the temperature range. A small inset graph emphasizes the peak responses at a magnified scale, providing a clearer view of the TZO and *a*TZO sensors' behavior. Fig. 7b illustrates the change in resistance over time when the sensors are exposed to NO gas at 200 °C. The gas sensor responses are quantified by percentages, with *i*TZO showing the highest response. In a shaded region indicating a period of NO exposure, the *i*TZO sensor demonstrates a dramatic increase in resistance (labeled with "$S = 1300$ %"), revealing a strong response to NO gas presence. The other two sensors show much smaller changes in resistance when exposed to NO gas. The gas sensor responses to NO gas exposure are quantified by percentages, with *i*TZO showing the highest response. This could be linked to the morphological and structural changes that cause a significant increase in the sensor's ability to detect the presence of NO gas [72,73]. As evidenced by the marked resistance change, the *i*TZO sensor's high sensitivity to NO gas may be attributed to its material composition and structural changes by IPIB irradiation that enhance NO gas interaction [74]. The TZO sensor exhibits a relatively flat response, suggesting lower sensitivity which could be due to the disorderly ohmic contact between the sensing layer and the IDT electrodes with high resistance (see Fig. 5b, $R_{TZO} \sim 9.27 \times 10^8$ Ω). Furthermore, Hall measurements indicate that the TZO sample has a significantly lower carrier concentration (7.5×10^{18} cm^{-3}) compared to *a*TZO (1.9×10^{19} cm^{-3}) and *i*TZO (7.92×10^{19} cm^{-3}) films.

The detailed analysis and conclusions drawn from these figures will encompass discussions on the sensing mechanisms, as well as the impact of various structural and compositional modifications on sensor performance. The long-term stability of the TZO gas sensors is also examined, with performance assessments conducted over one year as illustrated in **Fig. 7c.** In this figure, the response of TZO and *a*TZO sensors to NO gas declines significantly over the first six months, decreasing by 32 % and 15 % respectively, while the *i*TZO sensor demonstrates better stability with only a 12 % reduction. Throughout the latter half of the year, all sensors exhibit further decreases in response and stability. These deteriorations could be attributed to a variety of external factors, including variations in air humidity and pressure, as well as the degradation of the IDT on the sensing surface. Additionally, the alterations in material properties caused by ion irradiation may gradually diminish over time, adversely affecting the sensors' stability.

Fig. 7d depicts a radar plot illustrating the gas selectivity of TZO sensors to various gases. This figure demonstrates that *i*TZO exhibits a significantly higher response to NO than TZO and *a*TZO, indicating that ion beam irradiation enhances the sensor's affinity for NO gas. When exposed to NO gas, the sensory responses showed an upward spike, which reverted to baseline upon removing NO gas. This behavior is most pronounced in Fig. 7e, where the *i*TZO sensor, which had the highest sensitivity, is highlighted. Notably, the *i*TZO sensor maintained high sensitivity even as NO gas concentration decreased from 100 ppm to 1 ppm. The relationship between NO gas concentration and the sensory response of the fabricated *i*TZO sensor, extrapolated from dynamic measurements, is also presented in Fig. 7e. To elucidate further the gas selectivity and the enhancement observed in the *i*TZO sample relative to other samples, the gas sensing mechanism is detailed below, accompanied by chemical equations and schematic illustrations.

3.6. DFT calculations

To investigate the effects of creating defects in the material on gas sensing, we applied density functional theory. ZnO (100) non-polar surface was chosen to achieve an equal number of Zn and O atoms on the surface before doping Ti by substituting the Zn atoms on the surface. After we introduced 1-Zn and 2-O defects, no Ti defects were included in the calculations due to the low probability of Ti defect formation, as the concentration of Ti in the material is only 1 %. The pristine and defective surfaces were relaxed after an additional relaxation step with NO gas on the surface. The results reveal that the adsorption of NO occurs through the formation of a Ti-N bond on the surface of the material as shown in **Fig. 8(a,b).** On the pristine TZO material, following gas adsorption, the bonding length between Ti and O increases, and the Ti atom shifts towards the gas. Similarly, the adsorption energy is measured at 2.5 eV, indicating chemisorption. In contrast, the defective surface shows an adsorption energy of approximately −1.11 eV. The lowest adsorption energy of the system indicates the most stable interaction between the surface and the gas. In the field of gas sensors, a moderate level of surface-gas interaction energy is preferred. This is because high interaction energy within the sensor module can hinder the desorption of gas molecules from the surface. Such hindrance affects the sensor's ability to recover and impairs its reusability, as gas molecules may remain trapped on the surface. Shen et al. [41] demonstrated similar behavior of VOCs on both defective and pristine graphene-like ZnO materials. The authors claim that defect engineering can optimize the trade-off between adsorption energy strength and sensor performance.

3.7. Gas detection mechanism

The detection mechanism of gases using TZO sensors, specifically with NO, operates through a series of reactions explained by the widely accepted model for n-type semiconductors. In air environments at elevated temperatures, oxygen molecules are adsorbed onto the semiconductor's surface, altering the resistance of the TZO sensing material [75]. The electrons in the conduction band facilitate the reduction of O_2 into its ionic forms, predominantly forming O^- ions at 125 °C [76]. This accumulation of O^- ions on the surface of the TZO contributes to the development of a core-shell structure, where the core represents the semiconductor particle's interior and the shell is an electron depletion layer (DL) [77]. This layer forms as electrons are utilized in reducing O_2. The presence of the DL is inferred from AFM and XPS analyses, which reveal characteristic oxygen signals in the O 1 s spectra, as previously reported [17,78].

In our earlier studies [17,78], we conducted extensive investigations into the interaction of NO gas with ZnO and TZO nanostructures, employing numerous physical and chemical analytical methods. These studies demonstrated that the initial flux of NO_x primarily involves nitric oxide (NO), followed by nitrogen dioxide (NO_2), facilitated by various defects in the ZnO nanostructure's crystal lattice. The formation of adsorbed NO^- (ads) and NO_2^- (ads) may also occur through the involvement of electrons from the conduction zone of ZnO, lattice oxygen $O_{2(lat)}$ or adsorbed ions $O^-_{2(ads)}$ [77]:

$$NO_{gas} + e^- \leftrightarrow NO^- \tag{7}$$

$$NO_{gas} + 1/2O_{2(lat)} + e^- \leftrightarrow NO^-_{2\ (ads)} \tag{8}$$

$$NO_{gas} + O^-_{2(ads)} \leftrightarrow NO^-_{2\ (ads)} \tag{9}$$

After the formation of adsorbed $NO^-_{(ads)}$ and $NO^-_{2\ (ads)}$ on the ZnO surface, these groups undergo decomposition and desorption, influenced by various defects, resulting in the release of NO, N_2O, and NO_2 [79]. Additionally, IPIB (intense pulsed ion beam) irradiation promotes the recombination of electron-hole pairs, leading to the generation of additional reactive oxygen species. The liberated electrons (e^-) participate in reactions (7–9), while the formed O^- ions enhance the accumulation of adsorbed NO and NO_2 molecules on the ZnO surface. The generated holes (h^+) contribute to the decomposition of $NO^-_{(ads)}$ and $NO^-_{2\ (ads)}$ assisting in the desorption of these products via the following reactions:

$$NO^-_{gas} + h^+ \leftrightarrow NO_{gas} \tag{10}$$

$$2NO^-_{2(ads)} + 2h^+ \rightarrow 2NO_{2(gas)+}O_{2(gas)} \tag{11}$$

Thus, thermal and ion treatments enhance the intensity of the gas reactions (7–10) for the formation of NO^{-}_{gas} and $NO^{-}_{2(ads)}$ as well as their subsequent decomposition (reaction 11). These processes significantly improve the gas sensing performance of *a*TZO and *i*TZO sensors. The schematic illustration of the main gas sensing mechanism of *a*TZO and *i*TZO samples are provided in Fig. 8 and 9. The IPIB irradiation of MOS material can lead to the production of lattice defects such as vacancies, defects, and dislocations. These defects serve as recombination centers by trapping the electrons generated on the surface of the sensing material, which, in our case, are TZO nanostructures.

As shown in **Fig. 9(a-d)**, the schematic representation illustrates the surface modifications induced by thermal treatment and IPIB irradiation, highlighting their effects on the electrical contacts and active site distribution in modified TZO sensors. Fig. 9a depicts a bare TZO film deposited on a substrate, characterized by a low surface area. The film exhibits irregular contact with the IDTs, potentially affecting the efficiency of electronic conduction pathways. The surface, adorned with minimal adsorbed species (NO), offers limited active sites for surface interactions. Upon thermal annealing (Fig. 9b), *a*TZO exhibits a high RMS surface area, indicating increased physical irregularities. This alteration creates oxygen vacancies, enhancing the film's electronic properties and improving contact with IDTs. The process modifies the structural integrity and optimizes the surface for increased adsorption of reactive species, thus promoting enhanced active site availability. Meanwhile, the iTZO sensor exposed to IPIB irradiation resulted in the generation of new secondary particles, the appearance of significant structural defects, and an increase in the RMS surface area. This irradiation process catalyzes the formation of new chemical bonds and elevates the number of oxygen vacancies, markedly intensifying the number of active sites available for chemical reactions. The depicted C—H bonds (see FT-IR results, Fig. 4a) suggest the incorporation of organic functionalities, offering new pathways for ion migration and surface reactions as clearly illustrated in Fig. 9c. In addition, Fig. 9d provides a quantitative insight into the penetration depth of ions and their energy loss within the substrate post-IPIB treatment. The results are obtained by the stopping and range of ions in matter (SRIM) simulation [80]. The graph shows a significant energy loss peaking at around 1.5 μm (**Fig. S3**), corresponding with a substantial ion distribution. This profile underscores the impact of IPIB irradiation in enhancing the sensor's ability to facilitate deeper and more efficient ion penetration, essential for the creation of a more reactive and conductive film surface.

It is well-known that IPIB irradiation is an effective method for enhancing conductivity, which is expected to significantly improve the gas-sensing properties of the TZO sensors. IPIB irradiation on the MOS-based nanomaterials leads to the formation of lattice defects, including vacancies, defects, and dislocations, which serve as recombination centers by trapping generated electrons [37]. Furthermore, exposure to high levels of radiation (i.e., high current density above 10 A/cm^2) induces substantial changes in the structural, morphological, and electrical characteristics of the MOSs even at relatively low fluence of the beam ($8{\cdot}10^{12}$ protons/cm^2). Specifically, the IPIB irradiation influences the MOS-based nanomaterials in two important ways: (a) transient effects resulting from the generation of electron-hole pairs, and (b) permanent effects due to the bombardment of materials with frequently pulsed ion beams, which alter the crystal lattice structure (evidenced by XRD and PL). For these reasons, the IPIB irradiation of metal oxides is expected to significantly enhance their gas-sensing performance.

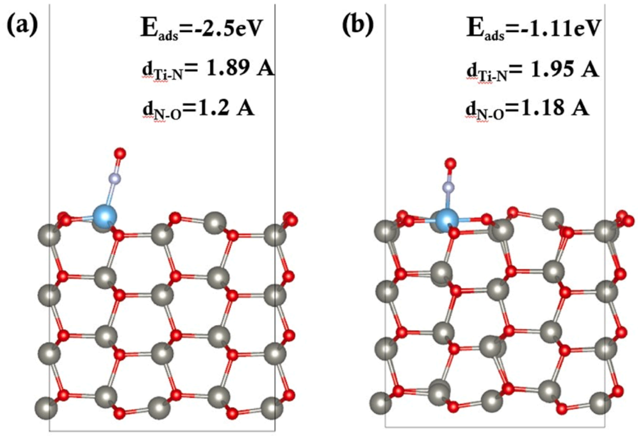

Fig. 8. Comparative illustration of NO gas adsorption on (a) pristine TZO and (b) TZO material with V_{Zn} and V_{O} defects.

This enhancement is attributed to oxygen vacancies [81], which serve as preferred adsorption sites for NO molecules [82]. However, an annealed *a*TZO sample reveals minimal oxygen defects, as evidenced by AFM, XPS, and PL analysis (see SI of PL results, **Fig. S4**). The low oxygen defect density on the *a*TZO sample surface diminishes its NO adsorption capacity. Conversely, the incorporation of Ti as a dopant in the *i*TZO sample introduces numerous electrons and significant oxygen defects, thus abolishing the depletion region and boosting conductivity. The oxygen-deficient surface of the *i*TZO samples adsorbs substantial amounts of NO, and the subsequent reaction with oxygen ions produces electrons that further enhance conductivity. Consequently, the gas sensing response of *i*TZO to NO is markedly higher than that of *a*TZO sample. For instance, at an NO concentration of 100 ppm, the carrier concentration in the *i*TZO sample increases to 7.91×10^{19} cm^{-3}, approximately four orders of magnitude greater than the 1.9×10^{19} cm^{-3} observed in *a*TZO. This significant increase in carrier concentration is attributed to the generation of carriers by the vacancies by IPIB treatment, indicating that the oxygen vacancy density in *i*TZO sample is substantially higher than in *a*TZO sample. This is also indicated by the significant increase in the PL peak of the green zone after irradiation [83,84].

4. Conclusions

In this study, the application of the Intensely Pulsed Ion Beam technique to enhance the gas-sensing properties of the TZO-based sensors has been successfully demonstrated. The investigations reveal that IPIB irradiation significantly modifies the surface morphology and crystalline structure of TZO nanostructures, thereby improving their sensitivity and selectivity to NO gas compared to other gases like CO, CO_2, NO_2, ethanol, methane, and acetone. The comparative analysis of TZO, *a*TZO, and *i*TZO samples illustrates that IPIB treatment not only enhances the roughness and porosity of the TZO films but also induces beneficial lattice defects and oxygen vacancies. These changes contribute to a marked increase in gas response, particularly for NO gas, where the *i*TZO sensor exhibits a response increase of approximately 1300 % at an optimal temperature of 200 °C. This substantial enhancement underscores the potential of IPIB with beam current density of about 12 A/cm^2 as a powerful tool for advancing the performance of MOS-based gas sensors even at relatively low fluence of $8{\cdot}10^{12}$ cm^{-2}. Furthermore, the stability tests conducted over a year demonstrate that the *i*TZO sensors maintain their enhanced sensitivity with minimal degradation, suggesting that the improvements induced by IPIB irradiation are durable and effective for long-term applications. This attribute is crucial for the development of reliable and efficient gas sensors required in environmental monitoring and industrial applications. Furthermore, DFT calculations reveal an increase in the volume of the crystal structure when protons are stopped in the material, and shrinkage of the crystal structure volume during annealing, which correlates with experimental results. Finally, our research highlights the significant advantages of using ion beam techniques like IPIB for the targeted modification of the gas sensor materials. The ability to precisely control the ion dose and energy allows for the optimization of sensor characteristics, paving the way for the next generation of highly sensitive and selective gas sensors. The outcomes of this study contribute

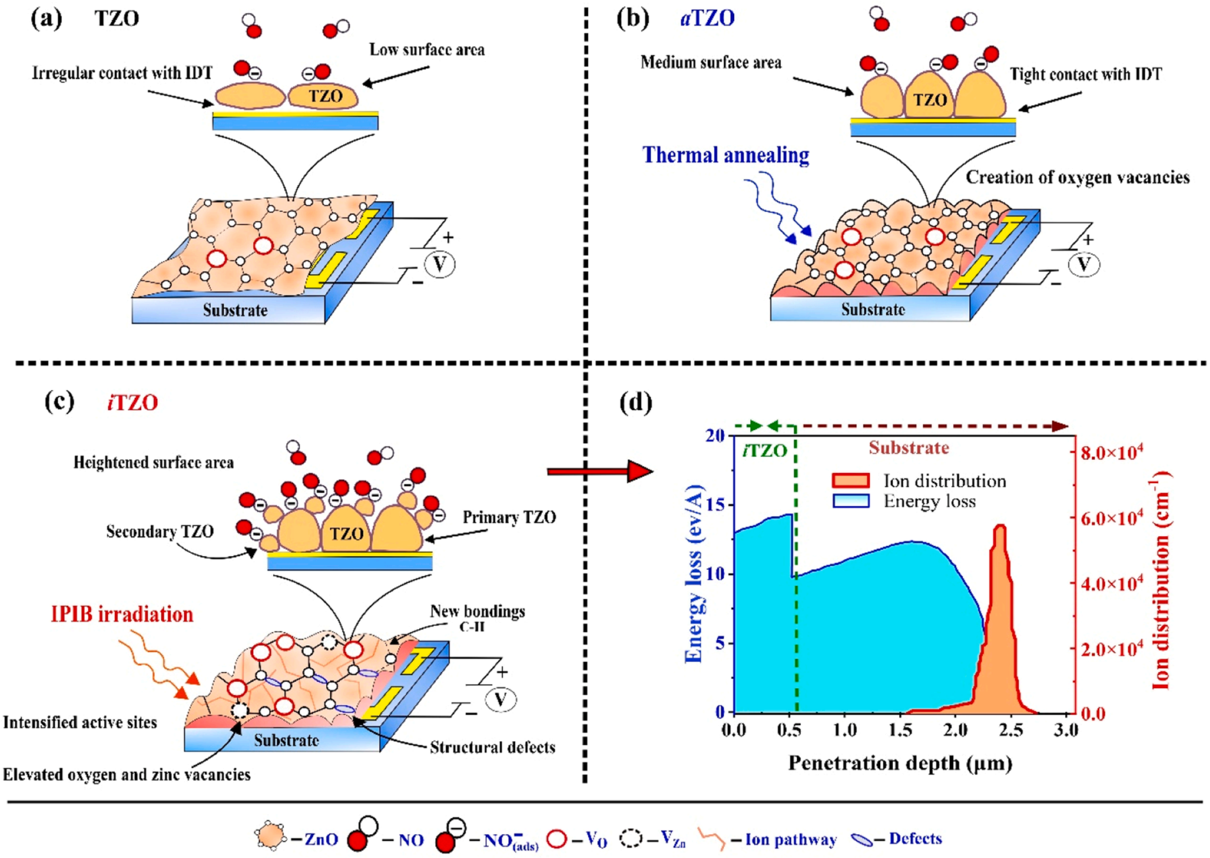

Fig. 9. Schematic illustration of the gas sensing mechanism of (a) TZO, (b) *a*TZO, and (c) *i*TZO sensors; (d) is the SRIM simulation of ion penetration depth.

valuable insights into the material science of gas sensors and open up new avenues for further research in sensor technology enhancement.

Ethics declarations

The authors state that they have no conflicting interests.

CRediT authorship contribution statement

Gani Yergaliuly: Writing – review & editing, Writing – original draft, Visualization, Software, Methodology, Investigation, Formal analysis, Data curation, Conceptualization. **Abylay Tangirbergen:** Writing – original draft, Visualization, Software, Methodology, Investigation, Data curation, Conceptualization. **Almagul Mentbayeva:** Writing – review & editing, Visualization, Validation, Resources, Funding acquisition, Formal analysis. **Nurlan Amangeldi:** Supervision, Resources, Investigation, Formal analysis, Data curation. **Marat Kaikanov:** Writing – review & editing, Visualization, Resources, Investigation, Conceptualization. **Selim Acar:** Writing – review & editing, Resources, Methodology, Investigation, Formal analysis, Data curation. **Zhumabay Bakenov:** Writing – review & editing, Validation, Supervision, Resources, Data curation. **Baktiyar Soltabayev:** Writing – review & editing, Writing – original draft, Validation, Software, Project administration, Investigation, Conceptualization.

Declaration of competing interest

The authors declare that they have no known competing financial interests or personal relationships that could have appeared to influence the work reported in this paper.

Acknowledgements

This research has been funded by the Science Committee of the Ministry of Science and Higher Education of the Republic of Kazakhstan (Grant No AP22785922).

The authors would like to express their sincere gratitude to Dr. Ahmad Ajjaq, a researcher at the Gas Sensors Laboratory of Gazi University, for his invaluable assistance in conducting NO gas sensitivity sensors experiments. We would also like to thank Mr. Almaz Beisenbayev, the research assistant at Nazarbayev University, for conducting PL analyses.

Supplementary materials

Supplementary material associated with this article can be found, in the online version, at doi:10.1016/j.apsadv.2025.100736.

Data availability

Data will be made available on request.

References

[1] P.S. J. Maximillian, M.L. Brusseau, E.P. Glenn, A.D. Matthias, Chapter 25 - pollution and environmental perturbations in the global system, in: M.L. Brusseau, I.L. Pepper, C.P.B.T -E, Third E. Gerba (Eds.), Chapter 25 - pollution and environmental perturbations in the global system, Acad. Press (2019) 457–476, https://doi.org/10.1016/B978-0-12-814719-1.00025-2.

[2] J.H.L. Ngai, Z. Li, J. Wang, J. He, J. Ding, Y. Li, Strategic design of Hemi-isoindigo polymer for a highly sensitive and selective all-printed flexible nitrogen dioxide chemiresistive sensor, Small Methods 8 (2024) 2301521, https://doi.org/10.1002/smtd.202301521.

[3] Y. Romero, N. Chicchon, F. Duarte, J. Noel, C. Ratti, M. Nyhan, Quantifying and spatial disaggregation of air pollution emissions from ground transportation in a

developing country context: case study for the Lima Metropolitan Area in Peru, Sci. Total Environ. 698 (2020) 134313, https://doi.org/10.1016/j.scitotenv.2019.134313.

[4] L. Wang, X. Chen, Z. Yi, R. Xu, J. Dong, S. Wang, Y. Zhao, Y. Liu, Facile synthesis of conductive metal−organic frameworks nanotubes for ultrahigh-performance flexible NO sensors, Small Methods 6 (2022) 1–10, https://doi.org/10.1002/smtd.202200581.

[5] M. Högman, P. Meriläinen, Extended NO analysis in asthma, J. Breath Res. 1 (2007) 24001, https://doi.org/10.1088/1752-7155/1/2/024001.

[6] R. Raddino, G. Caretta, M. Teli, I. Bonadei, D. Robba, G. Zanini, A. Madureri, S. Nodari, L.Dei Cas, Nitric oxide and cardiovascular risk factors, Heart Int. 3 (2007) 203, https://doi.org/10.1177/1826186807003001-203, 1826186807003001–.

[7] M. Amann, I. Bertok, J. Borken-Kleefeld, J. Cofala, C. Heyes, L. Höglund-Isaksson, Z. Klimont, B. Nguyen, M. Posch, P. Rafaj, R. Sandler, W. Schöpp, F. Wagner, W. Winiwarter, Cost-effective control of air quality and greenhouse gases in Europe: modeling and policy applications, Environ. Model. Softw. 26 (2011) 1489–1501, https://doi.org/10.1016/j.envsoft.2011.07.012.

[8] O. Pummakarnchana, N. Tripathi, J. Dutta, Air pollution monitoring and GIS modeling: a new use of nanotechnology based solid state gas sensors, Sci. Technol. Adv. Mater. 6 (2005) 251–255, https://doi.org/10.1016/j.stam.2005.02.003.

[9] T. Zhou, T. Zhang, Recent progress of nanostructured sensing materials from 0D to 3D: overview of structure–Property-application relationship for gas sensors, Small Methods 5 (2021) 2100515, https://doi.org/10.1002/smtd.202100515.

[10] A. Turlybekuly, Y. Shynybekov, B. Soltabayev, G. Yergaliuly, A. Mentbayeva, The Cross-sensitivity of chemiresistive gas sensors: nature, methods, and peculiarities: a systematic review, ACS Sens. 9 (2024) 6358–6371, https://doi.org/10.1021/acssensors.4c02097.

[11] M. Morais, E. Carlos, A. Rovisco, T. Calmeiro, H. Gamboa, E. Fortunato, R. Martins, P. Barquinha, Flexographic printed microwave-assisted grown zinc oxide nanostructures for sensing applications, Mater. Horizons (2024), https://doi.org/10.1039/D4MH01000K.

[12] K. Miyamoto, M. Sano, H. Kato, T. Yao, High-electron-mobility ZnO epilayers grown by plasma-assisted molecular beam epitaxy, J. Cryst. Growth 265 (2004) 34–40, https://doi.org/10.1016/j.jcrysgro.2004.01.035.

[13] X. Su, G. Duan, Z. Xu, F. Zhou, W. Cai, Structure and thickness-dependent gas sensing responses to NO2 under UV irradiation for the multilayered ZnO micro/nanostructured porous thin films, J. Colloid Interf. Sci. 503 (2017) 150–158, https://doi.org/10.1016/j.jcis.2017.04.055.

[14] F. Xu, C. Zhou, H.-P. Ho, A rule for operation temperature selection of a conductometric VOC gas sensor based on ZnO nanotetrapods, J. Alloys Compd. 858 (2021) 158294, https://doi.org/10.1016/j.jallcom.2020.158294.

[15] X. Chu, X. Zhu, Y. Dong, X. Ge, S. Zhang, W. Sun, Acetone sensors based on La3+ doped ZnO nano-rods prepared by solvothermal method, J. Mater. Sci. Technol. 28 (2012) 200–204, https://doi.org/10.1016/S1005-0302(12)60042-5.

[16] B. Soltabayev, Y. Raiymbekov, A. Nuftolla, A. Turlybekuly, G. Yergaliuly, A. Mentbayeva, Sensitivity enhancement of CO2 sensors at room temperature based on the CZO nanorod architecture, ACS Sens. 9 (2024) 1227–1238, https://doi.org/10.1021/acssensors.3c02059.

[17] B. Soltabayev, G. Yergaliuly, A. Ajjaq, A. Beldeubayev, S. Acar, Z. Bakenov, A. Mentbayeva, Quick NO gas sensing by Ti-doped flower–Rod-like ZnO structures synthesized by the SILAR method, ACS Appl. Mater. Interf. 14 (2022) 41555–41570, https://doi.org/10.1021/acsami.2c10055.

[18] R. Kajal, B.R. Kataria, K. Asokan, D. Mohan, Effects of gamma radiation on structural, optical, and electrical properties of SnO2 thin films, Appl. Surf. Sci. Adv. 15 (2023) 100406, https://doi.org/10.1016/j.apsadv.2023.100406.

[19] V. Misra, V. Singh, A. Singh, D. Kumar, S.K. Sharma, Photocatalytic degradation of methylene blue dye in aqueous solution under UV irradiation using NdMnO3:rGO hybrid nanocomposites as a photocatalyst, Appl. Surf. Sci. Adv. 18 (2023) 100491, https://doi.org/10.1016/j.apsadv.2023.100491.

[20] J.-H. Kim, A. Mirzaei, H.Woo Kim, P. Wu, S.S. Kim, Design of supersensitive and selective ZnO-nanofiber-based sensors for H2 gas sensing by electron-beam irradiation, Sens. Actuators B Chem. 293 (2019) 210–223, https://doi.org/10.1016/j.snb.2019.04.113.

[21] V. Chauhan, R. Kumar, Phase transformation and modifications in high-k ZrO2 nanocrystalline thin films by low energy Kr5+ ion beam irradiation, Mater. Chem. Phys. 240 (2020) 122127, https://doi.org/10.1016/j.matchemphys.2019.122127.

[22] S. Kaushik, S. Pandey, R. Singhal, R. Kumar, ZnO based RRAM performance enhancement by 100 MeV Ag9+ irradiation, Appl. Surf. Sci. Adv. 9 (2022) 100260, https://doi.org/10.1016/j.apsadv.2022.100260.

[23] G.A. El-Shobaky, A.S. Ahmad, M. Mokhtar, Effect of gamma-irradiation on surface and catalytic properties of CuO−ZnO/Al2O3 system, J. Radioanal. Nucl. Chem. 219 (1997) 89–94, https://doi.org/10.1007/BF02040271.

[24] S.M. Majhi, A. Mirzaei, S. Navale, H.W. Kim, S.S. Kim, Boosting the sensing properties of resistive-based gas sensors by irradiation techniques: a review, Nanoscale 13 (2021) 4728–4757, https://doi.org/10.1039/d0nr08448d.

[25] M.R. Waikar, P.M. Raste, R.K. Sonker, V. Gupta, M. Tomar, M.D. Shirsat, R. G. Sonkawade, Enhancement in NH3 sensing performance of ZnO thin-film via gamma-irradiation, J. Alloys Compd. 830 (2020) 154641, https://doi.org/10.1016/j.jallcom.2020.154641.

[26] G. Li, Z. Sun, D. Zhang, Q. Xu, L. Meng, Y. Qin, Mechanism of sensitivity enhancement of a ZnO nanofilm gas sensor by UV light illumination, ACS Sens. 4 (2019) 1577–1585, https://doi.org/10.1021/acssensors.9b00259.

[27] K.Y. Shin, A. Mirzaei, W. Oum, D.J. Yu, S. Kang, E.B. Kim, H.M. Kim, S.S. Kim, H. W. Kim, Enhancement of selective NO2 gas sensing via xenon ion irradiation of ZnO nanoparticles, Sens. Actuators B Chem. 374 (2023) 132808, https://doi.org/10.1016/j.snb.2022.132808.

[28] T. Schenkel, W. Redjem, A. Persaud, W. Liu, P.A. Seidl, A.J. Amsellem, B. Kanté, Q. Ji, Exploration of defect dynamics and color center Qubit synthesis with pulsed ion beams, Quantum Beam Sci. 6 (2022), https://doi.org/10.3390/qubs6010013.

[29] X.X. Mei, W.F. Sun, S.Z. Hao, T.C. Ma, C. Dong, Surface modification of high-speed steel by intense pulsed ion beam irradiation, Surf. Coatings Technol. 201 (2007) 5072–5076, https://doi.org/10.1016/j.surfcoat.2006.07.085.

[30] H. Zhong, J. Zhang, J. Shen, G. Liang, S. Zhang, M. Xu, X. Yu, S. Yan, G.E. Remnev, X. Le, Dynamic mechanism of crater formation induced by inclusion during intense pulsed ion beam irradiation, Vacuum 179 (2020) 109541, https://doi.org/10.1016/j.vacuum.2020.109541.

[31] X. Xiang, Z. He, J. Rao, Z. Fan, X. Wang, Y. Chen, Applications of ion beam irradiation in multifunctional oxide thin films: a review, ACS Appl. Electron. Mater. 3 (2021) 1031–1042, https://doi.org/10.1021/acsaelm.0c01071.

[32] A. Ates, M.A. Yıldırım, M. Kundakcı, A. Astam, Annealing and light effect on optical and electrical properties of ZnS thin films grown with the SILAR method, Mater. Sci. Semicond. Process. 10 (2007) 281–286, https://doi.org/10.1016/j.mssp.2008.04.003.

[33] S.P. Ratnayake, J. Ren, E. Colusso, M. Guglielmi, A. Martucci, E.Della Gaspera, SILAR deposition of metal oxide nanostructured films, Small 17 (2021) 2101666, https://doi.org/10.1002/smll.202101666.

[34] H.M. Pathan, C.D. Lokhande, Deposition of metal chalcogenide thin films by successive ionic layer adsorption and reaction (SILAR) method, Bull. Mater. Sci. 27 (2004) 85–111, https://doi.org/10.1007/BF02708491.

[35] G. Yergaliuly, B. Soltabayev, S. Kalybekkyzy, Z. Bakenov, A. Mentbayeva, Effect of thickness and reaction media on properties of ZnO thin films by SILAR, Sci. Rep. 12 (2022) 851, https://doi.org/10.1038/s41598-022-04782-2.

[36] M.M. Solovan, A.I. Mostovyi, H.P. Parkhomenko, M. Kaikanov, N. Schopp, E. A. Asare, T. Kovaliuk, P. Veřtát, K.S. Ulyanytsky, D.V. Korbutyak, V.V. Brus, A. High-Detectivity, Fast-response, and radiation-resistant TiN/CdZnTe heterojunction photodiode, Adv. Opt. Mater. 11 (2023) 2202028, https://doi.org/10.1002/adom.202202028.

[37] M. Kaikanov, A. Kemelbay, B. Amanzhulov, G. Demeuova, G. Akhtanova, F. Bozheyev, A. Tikhonov, Electrical conductivity enhancement of transparent silver nanowire films on temperature-sensitive flexible substrates using intense pulsed ion beam, Nanotechnology 32 (2021), https://doi.org/10.1088/1361-6528/abd49e.

[38] M. Kaikanov, B. Amanzhulov, G. Demeuova, G. Akhtanova, F. Bozheyev, A. Kemelbay, A. Tikhonov, Modification of silver nanowire coatings with intense pulsed ion beam for transparent heaters, Nanomaterials 10 (2020), https://doi.org/10.3390/nano10112153.

[39] B. Soltabayev, M.A. Yıldırım, A. Ateş, S. Acar, The effect of indium doping concentration on structural, morphological and gas sensing properties of IZO thin films deposited SILAR method, Mater. Sci. Semicond. Process. 101 (2019) 28–36, https://doi.org/10.1016/j.mssp.2019.05.026.

[40] Y. Shen, X. Zhao, Z. Cui, K. Qin, D. Ma, F. Cheng, P. Yuan, X. Qi, E. Li, First-principles investigation of the ZnO/TiSn2N4 heterojunction: a promising photoresponse material for high-performance photodetectors, Appl. Surf. Sci. 687 (2025) 162193, https://doi.org/10.1016/j.apsusc.2024.162193.

[41] Y. Shen, P. Yuan, Z. Yuan, Z. Cui, D. Ma, F. Cheng, K. Qin, H. Wang, E. Li, The O-defective g-ZnO sensor for VOC gases: the adsorption–Desorption, electronic, and sensitivity properties, Langmuir 40 (2024) 17396–17404, https://doi.org/10.1021/acs.langmuir.4c01491.

[42] G. Kresse, J. Hafner, Ab initio molecular dynamics for liquid metals, Phys. Rev. B 47 (1993) 558–561, https://doi.org/10.1103/PhysRevB.47.558.

[43] G. Kresse, J. Hafner, Ab initio molecular-dynamics simulation of the liquid-metalamorphous- semiconductor transition in germanium, Phys. Rev. B 49 (1994) 14251–14269, https://doi.org/10.1103/PhysRevB.49.14251.

[44] D. Joubert, From ultrasoft pseudopotentials to the projector augmented-wave method, Phys. Rev. B - Condens. Matter Mater. Phys. 59 (1999) 1758–1775, https://doi.org/10.1103/PhysRevB.59.1758.

[45] Y. Shen, X. Zhao, Z. Cui, K. Qin, D. Ma, F. Cheng, P. Yuan, X. Qi, E. Li, van der Waals ZnO/HfSn2N4 heterojunction with exceptional photoresponse for photodetectors, ACS Appl. Mater. Interf. 16 (2024) 58802–58810, https://doi.org/10.1021/acsami.4c10486.

[46] Y. Shen, P. Yuan, Z. Yuan, Z. Cui, D. Ma, F. Cheng, K. Yang, Y. Dong, E. Li, The electronic and optical properties of non-metallic doped g-C3N4/MoS2 heterojunction, Phys. B Condens. Matter. 674 (2024) 415583, https://doi.org/10.1016/j.physb.2023.415583.

[47] Y. Shen, P. Yuan, Z. Yuan, Z. Cui, D. Ma, F. Cheng, K. Qin, H. Wang, E. Li, Modulation of electronic and optical properties of g-CN/XTe2(X=W, Mo) heterojunctions by biaxial strain, Int. J. Hydrogen Energy 80 (2024) 289–297, https://doi.org/10.1016/j.ijhydene.2024.07.148.

[48] J.P. Perdew, K. Burke, M. Ernzerhof, Generalized gradient approximation made simple (vol 77, pg 3865, 1996), Phys. Rev. Lett. 78 (1997) 1396. –1396.

[49] C.N. Wang, Y.L. Li, F.L. Gong, Y.H. Zhang, S.M. Fang, H.L. Zhang, Advances in doped ZnO nanostructures for gas sensor, Chem. Rec. 20 (2020) 1553–1567, https://doi.org/10.1002/tcr.202000088.

[50] A.B.T.-R.R.A.P. J. Humphreys, G.S. Rohrer, A. Rollett, in: J. Humphreys, G. S. Rohrer, Third E. Rollett (Eds.), Chapter 1 - Introduction, Elsevier, Oxford, 2017, pp. 1–11, https://doi.org/10.1016/B978-0-08-098235-9.00001-X. A.B.T.-R.R.A.P.

[51] D.K. Sadana, Mechanisms of amorphization and recrystallization in ion implanted III–V compound semiconductors, Nucl. Instruments Methods Phys. Res. Sect. B Beam Interact. with Mater. Atoms 7–8 (1985) 375–386, https://doi.org/10.1016/0168-583X(85)90585-3.

[52] G.N. Van Wyk, H.J. Smith, Crystalline reorientation due to ion bombardment, Nucl. Instruments Methods 170 (1980) 433–439, https://doi.org/10.1016/0029-554X(80)91053-8.

[53] S. Mustapha, M.M. Ndamitso, A.S. Abdulkareem, J.O. Tijani, D.T. Shuaib, A. K. Mohammed, A. Sumaila, Comparative study of crystallite size using Williamson-Hall and Debye-Scherrer plots for ZnO nanoparticles, Adv. Nat. Sci. Nanosci. Nanotechnol. 10 (2019) 0–8, https://doi.org/10.1088/2043-6254/ab52f7.

[54] M.R. Parra, F.Z. Haque, Aqueous chemical route synthesis and the effect of calcination temperature on the structural and optical properties of ZnO nanoparticles, J. Mater. Res. Technol. 3 (2014) 363–369, https://doi.org/10.1016/j.jmrt.2014.07.001.

[55] Y.J. Tak, B. Du Ahn, S.P. Park, S.J. Kim, A.R. Song, K.-B. Chung, H.J. Kim, Activation of sputter-processed indium–gallium–zinc oxide films by simultaneous ultraviolet and thermal treatments, Sci. Rep. 6 (2016) 21869, https://doi.org/10.1038/srep21869.

[56] A. Perrotta, J. Pilz, A. Milella, A.M. Coclite, Opto-chemical control through thermal treatment of plasma enhanced atomic layer deposited ZnO: an in situ study, Appl. Surf. Sci. 483 (2019) 10–18, https://doi.org/10.1016/j.apsusc.2019.03.122.

[57] N. Rana, S. Chand, A.K. Gathania, Tailoring the structural and optical properties of ZnO by doping with Cd, Ceram. Int. 41 (2015) 12032–12037, https://doi.org/10.1016/j.ceramint.2015.06.017.

[58] A.G. Kaningini, S. Azizi, N. Sintwa, K. Mokalane, K.C. Mohale, F.N. Mudau, M. Maaza, Effect of optimized precursor concentration, temperature, and doping on optical properties of ZnO nanoparticles synthesized via a green route using Bush Tea (Athrixia phylicoides DC.) Leaf extracts, ACS Omega 7 (2022) 31658–31666, https://doi.org/10.1021/acsomega.2c00530.

[59] P. Maji, R.B. Choudhary, M. Majhi, Structural, electrical and optical properties of silane-modified ZnO reinforced PMMA matrix and its catalytic activities, J. Non. Cryst. Solids 456 (2017) 40–48, https://doi.org/10.1016/j.jnoncrysol.2016.10.039.

[60] P.V. Vardhan, L.I. Shukla, FT-IR investigations on effect of high doses of gamma radiation-induced damage to polystyrene and mechanism of formation of radiolysis products, Radiat. Environ. Biophys. 57 (2018) 301–310, https://doi.org/10.1007/s00411-018-0740-y.

[61] M.Ebrahimi Naghani, M. Neghabi, M. Zadsar, H.Abbastabar Ahangar, Synthesis and characterization of linear/nonlinear optical properties of graphene oxide and reduced graphene oxide-based zinc oxide nanocomposite, Sci. Rep. 13 (2023) 1496, https://doi.org/10.1038/s41598-023-28307-7.

[62] J.-Y. Ye, J.-L. Lin, Z.-Y. Zhou, Y.-H. Hong, T. Sheng, M. Rauf, S.-G. Sun, Ammonia electrooxidation on dendritic Pt nanostructures in alkaline solutions investigated by in-situ FTIR spectroscopy and online electrochemical mass spectroscopy, J. Electroanal. Chem. 819 (2018) 495–501, https://doi.org/10.1016/j.jelechem.2017.12.062.

[63] S. Senthilkumaar, K. Rajendran, S. Banerjee, T.K. Chini, V. Sengodan, Influence of Mn doping on the microstructure and optical property of ZnO, Mater. Sci. Semicond. Process. 11 (2008) 6–12, https://doi.org/10.1016/j.mssp.2008.04.005.

[64] M.R.Khan Wahiduzzaman, S. Harp, J. Neumann, Q.N. Sultana, Processing and performance of MOF (Metal Organic Framework)-loaded PAN nanofibrous membrane for CO2 adsorption, J. Mater. Eng. Perform. 25 (2016) 1276–1283, https://doi.org/10.1007/s11665-016-1966-y.

[65] K.Y. Ko, J.-G. Song, Y. Kim, T. Choi, S. Shin, C.W. Lee, K. Lee, J. Koo, H. Lee, J. Kim, T. Lee, J. Park, H. Kim, Improvement of gas-sensing performance of large-area tungsten disulfide nanosheets by surface functionalization, ACS Nano 10 (2016) 9287–9296, https://doi.org/10.1021/acsnano.6b03631.

[66] S. Yurdakal, C. Garlisi, L. Özcan, M. Bellardita, G. Palmisano, Chapter 4 - (Photo) catalyst characterization techniques: adsorption isotherms and BET, SEM, FTIR, UV–Vis, photoluminescence, and electrochemical characterizations, in: G. Marcì, L. B.T.-H.P. Palmisano (Eds.), Chapter 4 - (Photo)catalyst characterization techniques: adsorption isotherms and BET, SEM, FTIR, UV–Vis, photoluminescence, and electrochemical characterizations, Elsevier (2019) 87–152, https://doi.org/10.1016/B978-0-444-64015-4.00004-3.

[67] C. Rehermann, A. Merdasa, K. Suchan, V. Schröder, F. Mathies, E.L. Unger, Origin of ionic inhomogeneity in MAPb(IxBr1–x)3 perovskite thin films revealed by In-situ spectroscopy during spin coating and annealing, ACS Appl. Mater. Interf. 12 (2020) 30343–30352, https://doi.org/10.1021/acsami.0c05894.

[68] J. Zhang, X. Liu, S. Wu, B. Cao, S. Zheng, One-pot synthesis of Au-supported ZnO nanoplates with enhanced gas sensor performance, Sens. Actuators B Chem. 169 (2012) 61–66, https://doi.org/10.1016/j.snb.2012.02.070.

[69] L. Liu, Y. Wang, K. Guan, Y. Liu, Y. Li, F. Sun, X. Wang, C. Zhang, S. Feng, T. Zhang, Influence of oxygen vacancies on the performance of SnO2 gas sensing by near-ambient pressure XPS studies, Sens. Actuators B Chem. 393 (2023) 134252, https://doi.org/10.1016/j.snb.2023.134252.

[70] J. Wang, Z. Wang, B. Huang, Y. Ma, Y. Liu, X. Qin, X. Zhang, Y. Dai, Oxygen vacancy induced band-gap narrowing and enhanced visible light photocatalytic activity of ZnO, ACS Appl. Mater. Interf. 4 (2012) 4024–4030, https://doi.org/10.1021/am300835p.

[71] M. Al-Hashem, S. Akbar, P. Morris, Role of oxygen vacancies in nanostructured metal-oxide gas sensors: a review, Sens. Actuators B Chem. 301 (2019) 126845, https://doi.org/10.1016/j.snb.2019.126845.

[72] Q. Li, W. Zeng, Y. Li, Metal oxide gas sensors for detecting NO2 in industrial exhaust gas: recent developments, Sens. Actuators B Chem. 359 (2022) 131579, https://doi.org/10.1016/j.snb.2022.131579.

[73] G. Korotcenkov, The role of morphology and crystallographic structure of metal oxides in response of conductometric-type gas sensors, Mater. Sci. Eng. R Rep. 61 (2008) 1–39, https://doi.org/10.1016/j.mser.2008.02.001.

[74] N. Koshizaki, T. Oyama, Sensing characteristics of ZnO-based NOx sensor, Sens. Actuators B Chem. 66 (2000) 119–121, https://doi.org/10.1016/S0925-4005(00)00323-3.

[75] M.A. Franco, P.P. Conti, R.S. Andre, D.S. Correa, A review on chemiresistive ZnO gas sensors, Sens. Actuators. Rep. 4 (2022) 100100, https://doi.org/10.1016/j.snr.2022.100100.

[76] J. Zhang, Z. Qin, D. Zeng, C. Xie, Metal-oxide-semiconductor based gas sensors: screening, preparation, and integration, Phys. Chem. Chem. Phys. 19 (2017) 6313–6329, https://doi.org/10.1039/C6CP07799D.

[77] A.S. Mokrushin, I.A. Nagornov, T.L. Simonenko, N.P. Simonenko, P. Yu Gorobtsov, I.A. Arkhipushkin, E.P. Simonenko, V.G. Sevastyanov, N.T. Kuznetsov, Gas-sensitive nanostructured ZnO films praseodymium and europium doped: electrical conductivity, selectivity, influence of UV irradiation and humidity, Appl. Surf. Sci. 589 (2022) 152974, https://doi.org/10.1016/j.apsusc.2022.152974.

[78] B. Soltabayev, A. Ajjaq, G. Yergaliuly, Y. Kadyrov, A. Turlybekuly, S. Acar, A. Mentbayeva, Ultrasensitive nitric oxide gas sensors based on Ti-doped ZnO nanofilms prepared by RF magnetron sputtering system, J. Alloys Compd. 953 (2023) 170125, https://doi.org/10.1016/j.jallcom.2023.170125.

[79] M.-W. Ahn, K.-S. Park, J.-H. Heo, J.-G. Park, D.-W. Kim, K.J. Choi, J.-H. Lee, S.-H. Hong, Gas sensing properties of defect-controlled ZnO-nanowire gas sensor, Appl. Phys. Lett. 93 (2008) 263103, https://doi.org/10.1063/1.3046726.

[80] J.F. Ziegler, M.D. Ziegler, J.P. Biersack, SRIM – The stopping and range of ions in matter (2010), Nucl. Instruments Methods Phys. Res. Sect. B Beam Interact. Mater. Atoms 268 (2010) 1818–1823, https://doi.org/10.1016/j.nimb.2010.02.091.

[81] W. Kim, M. Choi, K. Yong, Generation of oxygen vacancies in ZnO nanorods/films and their effects on gas sensing properties, Sens. Actuators B Chem. 209 (2015) 989–996, https://doi.org/10.1016/j.snb.2014.12.072.

[82] M.J.S. Spencer, I. Yarovsky, ZnO nanostructures for gas sensing: interaction of NO2, NO, O, and N with the ZnO(101¯0) surface, J. Phys. Chem. C 114 (2010) 10881–10893, https://doi.org/10.1021/jp1016938.

[83] H. Shen, X. Shi, Z. Wang, Z. Hou, C. Xu, L. Duan, X. Zhao, H. Wu, Defects control and origins of blue and green emissions in sol-gel ZnO thin films, Vacuum 202 (2022) 111201, https://doi.org/10.1016/j.vacuum.2022.111201.

[84] M.A.K. Purbayanto, E. Nurfani, O. Chichvarina, J. Ding, A. Rusydi, Y. Darma, Oxygen vacancy enhancement promoting strong green emission through surface modification in ZnO thin film, Appl. Surf. Sci. 462 (2018) 466–470, https://doi.org/10.1016/j.apsusc.2018.08.170.